

Dendrite suppression of metal electrodeposition with liquid crystalline electrolytes

Zeeshan Ahmad^a, Zijian Hong^a, and Venkatasubramanian Viswanathan^{a,b,1}

^aDepartment of Mechanical Engineering, Carnegie Mellon University, Pittsburgh, Pennsylvania 15213, USA; ^bDepartment of Physics, Carnegie Mellon University, Pittsburgh, Pennsylvania 15213, USA

We study the dynamics of electrodeposition of a metal in contact with a liquid crystalline electrolyte. A nematic liquid crystalline electrolyte introduces an additional overpotential due to its bulk distortion and anchoring free energy. A phase-field model is built to simulate the morphological evolution of the metal anode under electrodeposition with nematic liquid crystal electrolyte. We provide design guidelines for achieving smooth electrodeposition with liquid crystalline electrolyte; in particular, we identify high anchoring energy can suppress dendrite growth. Liquid crystalline electrolytes offer a new avenue towards enabling high energy density rechargeable batteries based on metal anodes.

Lithium metal | Liquid Crystal | Batteries | Dendrites

Metal electrodeposition is a process of fundamental importance with applications ranging from generating surface coatings and multilayer thin films to designing functional nanomaterials (1–4). Recently, there is a great resurgence of interest in understanding electrodeposition as rechargeable batteries based on lithium (Li) metal anodes has emerged as a viable strategy for improving the energy density of Li-ion batteries. In addition, fast charging requirement in rechargeable batteries (5) requires electrodeposition at high rates which leads to the well-known dendritic instability (6).

Numerous approaches for suppressing dendritic growth have been proposed. These include artificial solid electrolyte interphase (SEI) (7–9), additives in liquid electrolytes (10–16), surface nanostructuring (17, 18), solid polymer or inorganic electrolytes (19–23). Among the many approaches, mechanical suppression of dendrite growth through stresses at solid-solid interfaces provides design principles for the desired mechanical properties for polymer and inorganic electrolytes (24–26). These analyses suggest that polymers with high shear modulus, while ceramics with low shear modulus can lead to stable electrodeposition. Generally, most polymers tend to be soft while ceramics tend to be hard and hence finding ceramic or polymer materials that satisfy the stability criterion has proved challenging (27).

Liquid crystalline materials offer an interesting new avenue to suppress dendritic growth through additional energetic contributions that emerge due to distortion and anchoring. These energies originate from the tendency of the anisotropic molecules to align resulting in an ordered arrangement (28). As compared to the other dendrite suppression methods, liquid crystals are easy to synthesize, manufacture and integrate into batteries, while offering the potential to suppress dendrites without external forces (e.g. stack pressure). Liquid crystal surface properties like anchoring energy are of importance in opto-electronic applications like liquid crystal displays, lithography and molecular electronics (29). Recently, Li-containing liquid crystalline materials have been developed as electrolytes possessing high ionic conductivity (30). In this work, we sim-

ulate electrodeposition of a metal anode in the presence of a liquid crystalline electrolyte. We find that liquid crystalline electrolytes with sufficient anchoring energy at the interface with the metal anode can greatly suppress dendrite growth. We quantify dendrite suppression using three metrics based on the shape and location of the interface and its growth with time. Based on this analysis, we provide design rules for material architectures that can meet this criterion.

Liquid crystalline phases are commonly found in materials composed of anisotropic molecules which interact with one another. In the simplest liquid crystalline phase called the nematic phase, molecules tend to orient parallel to each other giving rise to orientational order but no long range positional order. Engineered liquid crystalline materials are attractive candidates as electrolytes due to the presence of organized 1D, 2D or 3D pathways for ion conduction (30–34). Further, high transference number, low-cost bulk manufacturing, non-flammability and wider temperature window may be achieved in conjunction with fast ionic transport in the crystalline phase compared to amorphous phase (33, 35–37). Kerr et al. (34) and Sakuda et al. (38) obtained ionic conductivities in the range $10^{-6} - 10^{-3}$ S/cm at room temperature. Sakuda et al. (38) further demonstrated reversible charge-discharge cycling with LiFePO_4 and $\text{Li}_4\text{Ti}_5\text{O}_{12}$ cathodes and Li metal anode. While ionic conductivity and voltage stability of liquid crystalline electrolytes are promising, a natural question that emerges is whether liquid crystalline electrolytes in contact with a metal anode can suppress dendrites.

Fig. 1 shows a schematic of a metal anode in contact

Significance Statement

Lithium metal anodes offer a promising approach to improve the energy density of batteries to enable electrification of transportation. Dendrite suppression plagues the safety and cycle life of lithium metal anodes. Mechanical suppression of dendrites at solid-solid interfaces using ceramic and polymer electrolytes have been proposed, although it has proved to be challenging to realize high-efficiency systems with these classes of electrolytes. In this work, we suggest a new pathway through the use of liquid crystalline materials that can suppress dendrites due to their anchoring and elastic energies. We propose some techniques to increase the anchoring strength at the surface like nanopatterning required for practical applications in batteries.

Author Contributions: Z.A. and V.V. conceived the idea for the project. Z.A. and Z.H. developed the methodological framework. Z.A. ran the numerical simulations and all authors jointly wrote the manuscript.

The authors declare no conflict of interest.

¹To whom correspondence should be addressed. E-mail: venkvis@cmu.edu

with a nematic liquid crystalline electrolyte. The average orientation of the molecules is given by a unit vector \mathbf{n} called the director. In a distorted liquid crystal, the director will vary with space $\mathbf{n} = \mathbf{n}(r)$. The bulk distortion free energy of the liquid crystal can be written in terms of the director field \mathbf{n} using three elastic constants corresponding to splay, twist and bend deformations (28). In this work, we use the

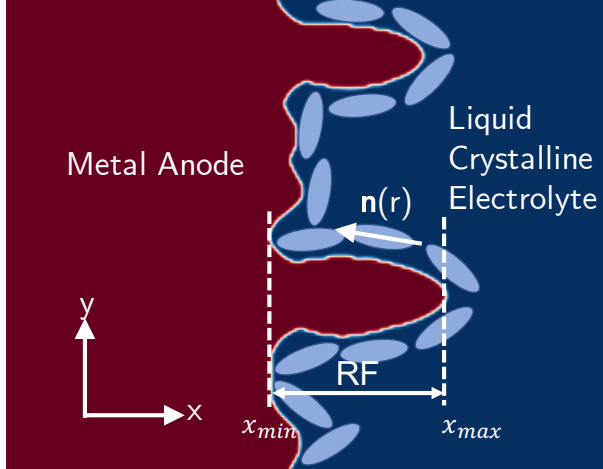


Fig. 1. Schematic of an interface between metal electrode and liquid crystalline electrolyte. $\mathbf{n}(r)$ is the director field of the liquid crystal. The liquid crystal molecules (size exaggerated) orient along the surface of the electrode due to anchoring energy.

one-constant approximation with elastic constant K which gives a simpler form of the distortion free energy as a volume integral:

$$F_d = \int dV \frac{1}{2} K (\nabla \mathbf{n} \cdot \nabla \mathbf{n}) \quad [1]$$

This form is easier to solve and gives valuable insights on distortions in nematics. Berreman used a similar form of the distortion free energy to explain the orientation of nematics in contact with a solid surface and grooved surface (39, 40). In addition to bulk distortion free energy, existence of an interface with the Li metal will result in certain preferred directions for the director of the molecules in contact (41). The preferred directions can be, for example, crystallographic directions for an interface with a single crystal or at a certain angle to the surface in the case of N-(4-methoxybenzylidene)-4-butyraniline (MBBA) free surface (28, 42). This results in the so called strong anchoring of the nematic phase at an interface. Here we use the form of anchoring energy derived from the expression proposed by Rapini and Papoular (43, 44) (details in Supplementary Information)

$$F_{\text{anch}} = \int dS \frac{1}{2} W (\mathbf{n} \cdot \mathbf{v})^2 \quad [2]$$

where \mathbf{v} is the normal to the interface between the electrode and the liquid crystalline electrolyte, W is the anchoring energy and the integration is performed over the interface area. This energy favors alignment of the liquid crystal molecules along the tangent to the interface.

Since the morphological evolution of the metal anode under electrodeposition involves moving interfaces, diffuse interface methods like phase-field model are ideal to treat the problem (45). A phase-field model is an efficient simulation tool

to obtain mesoscale insights on phase transitions, transformations and microstructural evolution (46–48). Previously, several phase-field simulation models have been developed for obtaining a quantitative understanding of dendrite growth in Li-ion batteries (49–53). Here we use the fully open source MOOSE (Multiphysics Object-Oriented Simulation Environment) framework (54) to solve the phase-field equations (55).

Phase-Field Model

Our phase-field model is based on Plapp's model (56) that unifies the thin interface formulations by using the grand potential functional to generate the phase-field equations. This formulation permits the use of a larger interface thickness parameter δ for computational convenience, much greater than the physical width of the interface while eliminating the non-physical effects. The phase-field variable ξ is a nonconserved order parameter whose value is 1 for the metal anode (solid) and 0 for the electrolyte (liquid). We use the Butler Volmer - Allen Cahn reaction (BV-ACR) equation for the evolution of the phase-field variable ξ with time t (49, 52, 53):

$$\frac{\partial \xi}{\partial t} = -\mathcal{M}_\sigma [g'(\xi) - \kappa \nabla^2 \xi] - \mathcal{M}_\eta h'(\xi) f(\eta) - q \quad [3]$$

where \mathcal{M}_σ and \mathcal{M}_η are the interfacial mobility and electrochemical reaction kinetics coefficient respectively. $g(\xi) = b\xi^2(1 - \xi^2)$ is a double-well function where b is related to the switching barrier and κ is the gradient energy coefficient. The surface energy γ and interface thickness δ can be used to obtain the values of $b = 12\gamma/\delta$ and $\kappa = 3\delta\gamma/2$ (50, 57). $h(\xi) = \xi^3(6\xi^2 - 15\xi + 10)$ is the interpolation function for ξ . A Langevin noise term q is added to the equation to account for thermal and structural fluctuations. $f(\eta)$ is related to the kinetics of electrodeposition in terms of the total overpotential η at the interface. The overpotential and hence the kinetics is modified by the liquid crystal due to a change in equilibrium potential difference between the electrode and the electrolyte. Let η_0 be the overpotential without the liquid crystal and η_{LC} be the additional overpotential due to the liquid crystal i.e. $\eta_{LC} = \eta - \eta_0$. The charge transfer coefficient for the liquid crystal overpotential η_{LC} will in general be different from that for η_0 (25, 58–61). Assuming a Butler Volmer equation with charge transfer coefficients α_c , α_a for the cathode and anode, and a cathodic charge transfer coefficient α_d for the liquid crystal overpotential, we obtain:

$$f(\eta) = \frac{c_{\text{Li}^+}}{c_0} \exp \left[-\frac{\alpha_d n \mathcal{F} \eta_{LC}}{RT} \right] \exp \left[-\frac{\alpha_c n \mathcal{F} \eta_0}{RT} \right] - \exp \left[\frac{(1 - \alpha_d) n \mathcal{F} \eta_{LC}}{RT} \right] \exp \left[\frac{\alpha_a n \mathcal{F} \eta_0}{RT} \right] \quad [4]$$

Parameters n , \mathcal{F} , R and T are the number of electrons transferred, Faraday's constant, gas constant and temperature respectively. The overpotential η can be written in terms of the potential at the anode (ϕ_e) and the electrolyte ϕ as $\eta = (\phi_e - \phi) - (\phi_e - \phi)_{\text{eqbm}}$. c_{Li^+} is the mole fraction of Li and c_0 is its standard mole fraction. The charge transfer coefficient α_d can be associated with mechanical deformation and heterogeneity at the interface. It is related to the parameter α_m introduced by Monroe and Newman (59) as $\alpha_d = 1 - \alpha_m$ and the parameters δ^{etrode} and δ^{elyte} used by McMeeking et

al. (60). Diggle et al. (58) found the value of α_m to be 1, giving $\alpha_d = 0$. In this work, we have used $\alpha_d = 0$ and $\alpha_a = \alpha_c = 0.5$. Simulations performed using $\alpha_d = 1$ did not show any noticeable difference in the evolution of the morphology as evident from Fig. S3.

The calculation of η_{LC} requires a model for the free energy of the liquid crystal. A liquid crystalline material in the electrolyte introduces an additional grand free energy given by

$$\Omega_{LC}[\xi] = \int dV \left[\frac{1}{2} K (\nabla \mathbf{n})^2 + \chi (\mathbf{n} \cdot \nabla \xi)^2 \right] [1 - h(\xi)] \quad [5]$$

Here χ is the anchoring energy factor accounting for the strong anchoring for the liquid crystal against the surface of the anode. The factor $1 - h(\xi)$ ensures that the liquid crystal free energy is non-zero only in the electrolyte phase. The second term is active only at the interface due to the presence of $\nabla \xi$. Using the fact that $|\nabla \xi| \sim 1/\delta$ at the interface and comparing the integral of the second term in Eq. (5) with Eq. (2), we obtain $\chi \sim W\delta/2$. This can be used to obtain estimates of χ since measured values for W for different liquid crystals are available in literature (62). The additional overpotential due to the liquid crystal can be calculated from its grand free energy contribution using Eq. 6 (50)

$$\frac{n\mathcal{F}}{V_{M^{z+}}} \eta_{LC} = \frac{\delta \Omega_{LC}}{\delta \xi} = \frac{\partial \Omega_{LC}}{\partial \xi} - \frac{\partial \Omega_{LC}}{\partial \nabla \xi} \quad [6]$$

where $V_{M^{z+}}$ is the molar volume of the metal in the liquid crystalline electrolyte. From this equation, we note that the molar volume accounts for the mole fraction share of energy of Li ion out of the total liquid crystal energy. Since liquid crystal relaxation occurs at a time scale much lower than the time scale of diffusion and electrodeposition, we assume equilibrium of the liquid crystal director field in the electrolyte i.e. $\delta \Omega_{LC}/\delta \mathbf{n} = 0$. The constraint $\mathbf{n} \cdot \mathbf{n} = 1$ on the director field is enforced by the hard constraint method utilizing the Lagrange multiplier technique (55). Together with evolution equation for the phase-field variable Eq. (3), the equations for the evolution of the chemical potential of Li and spatial distribution of the electric potential are also solved and are given in the Supplementary Information.

Results & discussion

A smooth 20 μm thick Li electrode is used as the initial configuration for the anode upon which Li is electrodeposited. The low initial thickness ensures that the cell has a high energy density due to the high fraction of Li passed per cycle (63, 64). The simulation parameters together with the details of the initial and boundary conditions are provided in the Supplementary Information. We used three metrics to quantify the dendrite growth or suppression during the morphological evolution of the electrode. The first metric, roughness factor is a measure of the unevenness of the Li electrode surface during electrodeposition. A perfectly smooth surface will have a value of zero whereas a surface with dendritic growth will have a high value of roughness factor. The roughness factor RF measures the range of the coordinate profile of the interface. For Fig. 1, the roughness factor is $\text{RF} = x_{\max} - x_{\min}$. This is one of the definitions of arithmetic average roughness of a surface. The second metric is the time required to cause short circuit (65) at a given x-coordinate in the 2D mesh.

For a given x-coordinate, the short circuit time t_{sc} is defined as the time when the metal electrode surface reaches that x-coordinate. This gives an indication of the time to short circuit the battery if the counter-electrode was located at that coordinate. The third metric used is related to the arc length of the interface between the metal electrode and the electrolyte. When the deposition is uneven, the arc length of the interface treated as a curve in two dimensions increases. We measure this deviation using the arc length ratio parameter $\tilde{L} = L/L_0$ where L is the length of the interface at a given time calculated by using the arc length formula for a curve and L_0 is the initial length of the interface ($= 200 \mu\text{m}$ in our simulations). Besides quantifying the deviation from an ideal interface, the arc length ratio is also related to the amount of Li consumed due to additional solid electrolyte interphase (SEI) growth at the non-ideal interface resulting in lowering of Coulombic efficiency. In the calculation of these metrics, we used the contour line $\xi = 0.5$ as the interface between the two phases.

We simulated electrodeposition on Li metal anode for the two cases of a conventional liquid electrolyte using the properties of 1 M LiPF_6 in EC:DMC (1:1 volume ratio) solution (hereafter referred to as the standard electrolyte) and a liquid crystalline electrolyte (hereafter referred to as the LC electrolyte). The properties of the electrolytes are given in Supplementary Information. For the sake of comparison, we assume the dimensionless values of the elastic constant and the anchoring energy to be $\tilde{K} = 2\tilde{\delta}^2 \tilde{R}\tilde{T}/\tilde{V}_{\text{Li}^+} = 39.3$ and $\tilde{W} = 20$. Although LC electrolytes may be engineered to have anisotropic diffusivity (66), we use isotropic diffusivity here for comparison with a standard electrolyte. Fig. 2a shows the variation of maximum x-coordinate of the metal electrode surface and the roughness factor as a function of time (black and blue lines respectively). For the case of a standard electrolyte, the metal electrode surface initially grows at a constant velocity with zero roughness factor. The surface starts to roughen at $t \sim 100$ s or when 20 μm Li has been deposited ($x \sim 40 \mu\text{m}$ at the interface), and the growth rate of the metal starts increasing due to high electric field and Li^+ concentration at the tip of the dendrites (53). In contrast, for the case of LC electrolyte, the surface remains uniform even till $t \sim 300$ s or when 90 μm of Li has been deposited. We observe that once the surface becomes rough and electrodeposition become dendritic in Fig. 2a, the growth rate increases rapidly since the deposition gets focused at the dendrite tips. Therefore, after the onset of dendritic growth, the maximum x-coordinate of the metal electrode surface at a given time is different in the case of a standard electrolyte and an LC electrolyte. For comparing the other two metrics, we used their values when the metal electrode surface has attained the same maximum x-coordinate rather than at the same time. Fig. 2b shows the variation of the arc length ratio \tilde{L} as a function of the maximum x-coordinate that the metal electrode surface has reached. With a standard electrolyte (black line), the interface arc length ratio quickly becomes greater than one as the metal electrode surface reaches 40 μm due to growth of surface perturbations. For 40 $\mu\text{m} \lesssim x \lesssim 80 \mu\text{m}$, several perturbations are generated at the metal electrode surface leading to a positive slope of the \tilde{L} vs x plot. As the metal electrode surface reaches 80 μm (60 μm of Li deposition), these perturbations lead to the growth of three dendrites (movie S1). This leads to an

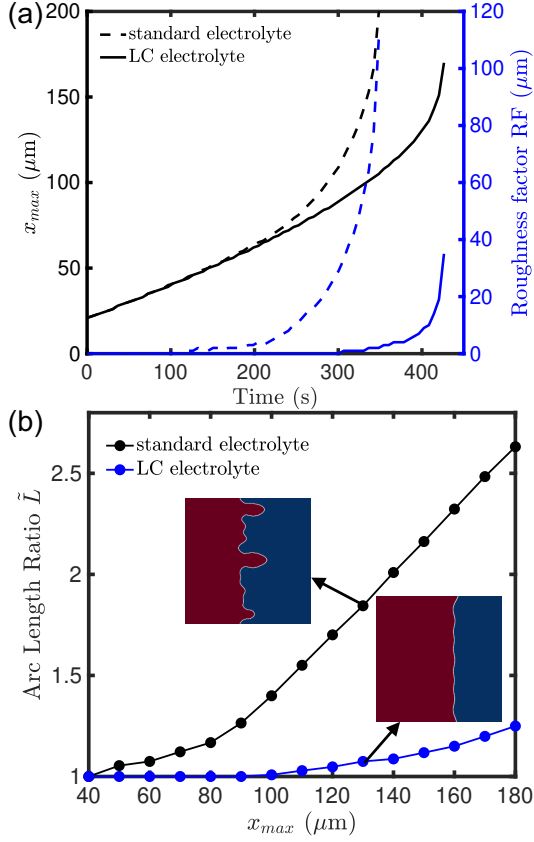


Fig. 2. Metal electrode surface growth with a standard and an LC electrolyte. The LC electrolyte has non-dimensional values of elastic constant $\tilde{K} = 39.3$ and anchoring energy $\tilde{W} = 20$. (a) Evolution of the metal electrode surface over time measured using the maximum x-coordinate of the interface. Metal electrode surface roughness (in blue) is quantified using the roughness factor $RF = x_{max} - x_{min}$ of the interface. (b) The interface arc length ratio measured as the ratio of the length of the interface to the length of the ideal interface is plotted versus x_{max} . The arc length ratio increases rapidly due to the development of dendritic peaks with a standard electrolyte which are suppressed in an LC electrolyte. The insets show the morphology of the metal surface at $x_{max} = 130 \mu\text{m}$.

increased slope of the \tilde{L} vs x_{max} curve in Fig. 2b. For the case of an LC electrolyte, the interface arc length remains close to the initial value till $x \sim 100 \mu\text{m}$ or for $80 \mu\text{m}$ of electrodeposition. After this point, there is a small increase in the arc length ratio due to generation of small surface perturbations, however, none of the perturbations are observed to grow into large dendrites (movie S2).

The discussion above clearly provides a compelling demonstration of the dendrite suppressing nature of LC electrolytes. The liquid crystal is able to suppress the small perturbations at the surface through a delicate interplay between distortion free energy, oxidation and reduction processes. In contrast to the standard electrolyte, we do not observe high current density hotspots during electrodeposition with an LC electrolyte at the interface. The existence of sharp peaks or valleys on the surface will result in sudden change in the orientation of the director field due to the strong anchoring boundary condition at the interface. This will result in an unfavorable high energy configuration of the director field. Our results confirm that it is possible to suppress dendrite growth and enhance the fraction of Li passed during cycling using an LC electrolyte.

Nucleation- To understand the rearrangement of the direc-

tor field at a rough surface and its effects on electrodeposition, we generate an initial perturbation on the the metal electrode surface and simulate electrodeposition under an applied overpotential. The perturbation is a hemispherical nucleus with three different radii: $5 \mu\text{m}$, $10 \mu\text{m}$ and $20 \mu\text{m}$ generated by setting the initial condition for the phase-field variable $\xi = 0$ inside the hemisphere. The director field of the liquid crystal reorients in response to the perturbation of the metal electrode surface (Fig. S2). Due to anchoring energy of the LC electrolyte, the director field becomes tangent to the metal electrode surface at the interface. The director field in the bulk also changes to minimize the distortion free energy proportional to the bulk elastic constant. Fig. 3a shows the maximum x-coordinate and roughness of the metal surface with time for the standard and LC electrolyte. The insets show the initial condition and the metal surface after 120 s of electrodeposition. Electrodeposition with the standard electrolyte leads to the development of sharp peaks from the initial nucleus. These peaks originate from the high current hotspots and encourage faster electrodeposition by attracting metal ions due to the high electric fields generated. The LC electrolyte prevents the formation of sharp peaks at the interface due to the anchoring energy, leading to an approximately constant growth velocity at the metal surface. The function $\mathcal{M}_\eta h'(\xi)f(\eta)$, which is the growth rate of the metal surface due to the overpotential, is plotted for the standard and LC electrolyte in Fig. S4 at $t = 31$ s. The standard electrolyte case has a more localized brown region at the tip of the hemisphere, showing a high current density hotspot compared to the LC electrolyte case. This point is elucidated in Fig. 3b showing the maximum of the metal surface growth rate due to overpotential, $\mathcal{M}_\eta h'(\xi)f(\eta)$ at each y-coordinate in the 2D domain. The maximum in the growth rate for a given y-coordinate occurs at the interface where the electrodeposition reaction occurs. The growth rate for the standard electrolyte is much more localized at the tip of the nucleus ($y = 100 \mu\text{m}$) compared to that for an LC electrolyte. The arc length ratio plotted as a function of the maximum x-coordinate of the metal surface for different initial nucleus radii also increases faster for the standard electrolyte compared to the LC electrolyte (Fig. S7). Fig. 3c shows the variation of the arc length ratio at $x_{max} = 160 \mu\text{m}$ with the radius of the nucleus. The arc length ratio obtained using an LC electrolyte decreases as the size of the initial perturbation decreases while it remains almost constant with a standard electrolyte. This variation can be used to determine the initial roughness of the metal anode sample to design for a given thickness of electrodeposited metal and final roughness/arc length ratio that can be tolerated.

To understand the effect of liquid crystal parameters - the elastic constant and anchoring energy on the metrics for dendrite suppression, we performed phase-field simulations using a range of values of the parameters K and W . Fig. 4 shows the variation of two metrics, roughness factor RF and interface arc length ratio \tilde{L} with the values of these parameters. The variation of short circuit time \tilde{t}_{sc} is presented in Fig. S8. The roughness factor, arc length ratio and short circuit time are calculated when the metal electrode surface reaches $x = 90, 120$ and $150 \mu\text{m}$ respectively. The roughness factor is represented in non-dimensional form as a ratio of its value obtained using LC electrolyte to the that obtained with a standard electrolyte. For all metrics, we observe that the den-

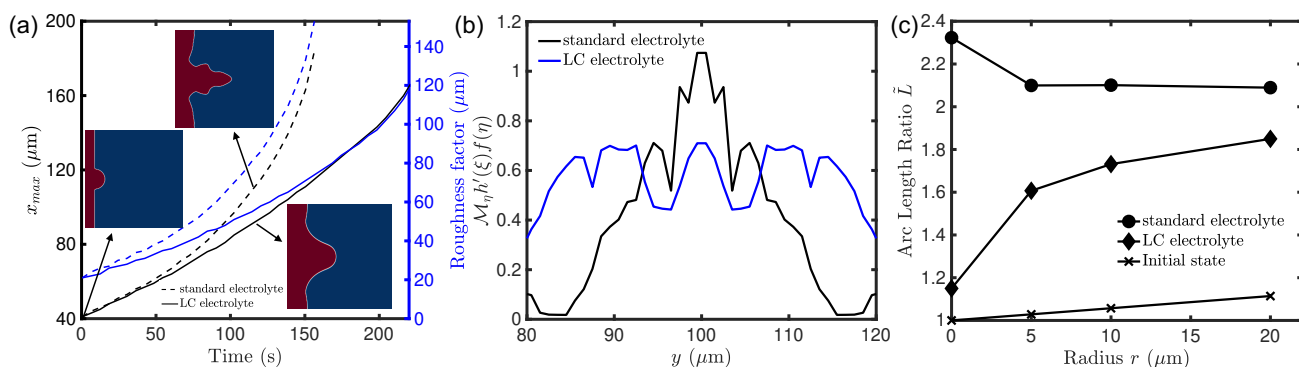


Fig. 3. Evolution of a hemispherical nucleus at the metal surface with a standard and an LC electrolyte. The LC electrolyte has values of elastic constant $\tilde{K} = 39.3$ and anchoring energy $\tilde{W} = 20$. (a) Evolution of maximum x-coordinate (black line) and roughness factor (blue line) of the metal electrode surface for $r = 20 \mu m$. The growth of the metal electrode surface with LC electrolyte (solid line) remains approximately linear while the growth with a standard electrolyte (dashed line) is much faster. The insets show the initial condition and morphology after 120 s. (b) Maximum value of growth rate at a y-coordinate for a standard and LC electrolyte after 31 s for $r = 20 \mu m$. The standard electrolyte has highly localized peaks of current density compared to the LC electrolyte. (c) Comparison of arc length ratio for different initial nucleus radii r at the metal surface at $x_{max} = 160 \mu m$. The LC electrolyte is more effective at suppressing dendrites for smaller initial surface perturbations.

drite suppression capability is improved as the elastic constant and the anchoring energy of the LC electrolyte is increased. From the plot, we observe that the anchoring energy W affects the metrics for dendrite suppression more than the bulk elastic constant. The arc length ratio of 1.5 is plotted as a contour line in Fig. 4b. The region to the right of the line has better dendrite suppression capability. A higher elastic constant further enhances the region of stability. Values of the elastic constant for some common liquid crystals are given in Table S3. The anchoring energy of nematic 5CB (4-n-pentyl-4-cyano biphenyl) at its interface with H-terminated (001) crystalline silicon surface and vacuum (67) is $\sim 0.14 \text{ J/m}^2$ ($\tilde{W} \sim 5.5 \times 10^{-2}$). Further work is needed to obtain values of anchoring energy for interface with Li. Although a limited dendrite suppression can be achieved using these parameters, an increase in the anchoring energy by one or two orders of magnitude would be more suitable for battery applications. It is worth noting that liquid crystalline properties can be changed by temperature (28), engineering the density of packing or particle shapes (68). These can lead to the emergence of directional entropic forces that align neighboring particles. Weng et al. reported an increase in anchoring energy by using vertical alignment and polymerized surfaces generated by ultraviolet irradiation-induced phase separation (69). Further, nanopatterning of the surfaces using surface lithography can lead to generation of nanogrooves which can be used to tune the anchoring energy strength (70, 71). The dendrite suppression metrics can be further improved by increasing the molar volume of Li in the LC electrolyte (Fig. S9).

Conclusions

In this work, we have suggested a potentially new material class, liquid crystalline materials, as candidate electrolytes for Li metal anodes. Additional energetic contributions due to anchoring and distortion provides a new approach to suppressing the onset of dendrite formation. Using phase-field simulations, we demonstrate enhanced dendrite suppression with liquid crystalline electrolytes. We identify the anchoring energy as an important tuning property that determines the degree of dendrite suppression as suggested by the values of the metrics. Our model is sufficiently general and the choice of the

preferred anchoring direction in Eq. 2 has no consequence on the dendrite suppression capability as long as there exists one preferred direction. The results of simulations with an initial perturbation can be used to design the initial roughness of the metal anode sample to be used. Finally, we suggest material design strategies that could achieve the high anchoring energy required for dendrite suppression in practical applications.

Materials and Methods

Code is available at <https://github.com/ahzeeshan/electrodep>.

ACKNOWLEDGMENTS. The authors thank Y.-M. Chiang, B.A. Helms and P.D. Frischmann for helpful discussions. Z.A. and V.V. acknowledge support from the Advanced Research Projects Agency Energy (ARPA-E) under Grant DE-AR0000774.

- YD Gamburg, G Zangari, *Theory and Practice of Metal Electrodeposition*. (Springer, New York, New York), (2011).
- C Ross, Electrodeposited multilayer thin films. *Annu. Rev. Mater. Sci.* **24**, 159–188 (1994).
- G Zhu, et al., Triboelectric-generator-driven pulse electrodeposition for micropatterning. *Nano Lett.* **12**, 4960–4965 (2012).
- A Robertson, U Erb, G Palumbo, Practical applications for electrodeposited nanocrystalline materials. *Nanostruct. Mater.* **12**, 1035–1040 (1999).
- S Ahmed, et al., Enabling fast charging – a battery technology gap assessment. *J. Power Sources* **367**, 250–262 (2017).
- W Xu, et al., Lithium metal anodes for rechargeable batteries. *Energy Environ. Sci.* **7**, 513–537 (2014).
- Q Liu, et al., Artificial protection film on lithium metal anode toward long-cycle-life lithium-oxygen batteries. *Adv. Mater.* **27**, 5241–5247 (2015).
- K Yan, et al., Ultrathin two-dimensional atomic crystals as stable interfacial layer for improvement of lithium metal anode. *Nano Lett.* **14**, 6016–6022 (2014).
- Y Liu, et al., An artificial solid electrolyte interphase with high li-ion conductivity, mechanical strength, and flexibility for stable lithium metal anodes. *Adv. Mater.* **29**, 1605531 (2017).
- D Aurbach, B Markovsky, A Shechter, Y Ein-Eli, H Cohen, A comparative study of synthetic graphite and li electrodes in electrolyte solutions based on ethylene carbonate-dimethyl carbonate mixtures. *J. Electrochem. Soc.* **143**, 3809–3820 (1996).
- T Hirai, I Yoshimatsu, J Yamaki, Effect of additives on lithium cycling efficiency. *J. Electrochem. Soc.* **141**, 2300–2305 (1994).
- F Ding, et al., Dendrite-free lithium deposition via self-healing electrostatic shield mechanism. *J. Am. Chem. Soc.* **135**, 4450–4456 (2013).
- J Qian, et al., High rate and stable cycling of lithium metal anode. *Nat. Commun.* **6**, 6362 (2015).
- L Suo, YS Hu, H Li, M Armand, L Chen, A new class of solvent-in-salt electrolyte for high-energy rechargeable metallic lithium batteries. *Nat. Commun.* **4**, 1481 (2013).
- Y Lu, Z Tu, LA Archer, Stable lithium electrodeposition in liquid and nanoporous solid electrolytes. *Nat. Mater.* **13**, 961 (2014).
- X Zhang, X Cheng, X Chen, C Yan, Q Zhang, Fluoroethylene carbonate additives to render uniform li deposits in lithium metal batteries. *Adv. Funct. Mater.* **27**, 1605989 (2017).
- D Wang, et al., Towards high-safe lithium metal anodes: Suppressing lithium dendrites via tuning surface energy. *Adv. Sci.* **4**, 1600168 (2017).
- Y Zhang, et al., Dendrite-free lithium deposition with self-aligned nanorod structure. *Nano Lett.* **14**, 6889–6896 (2014).

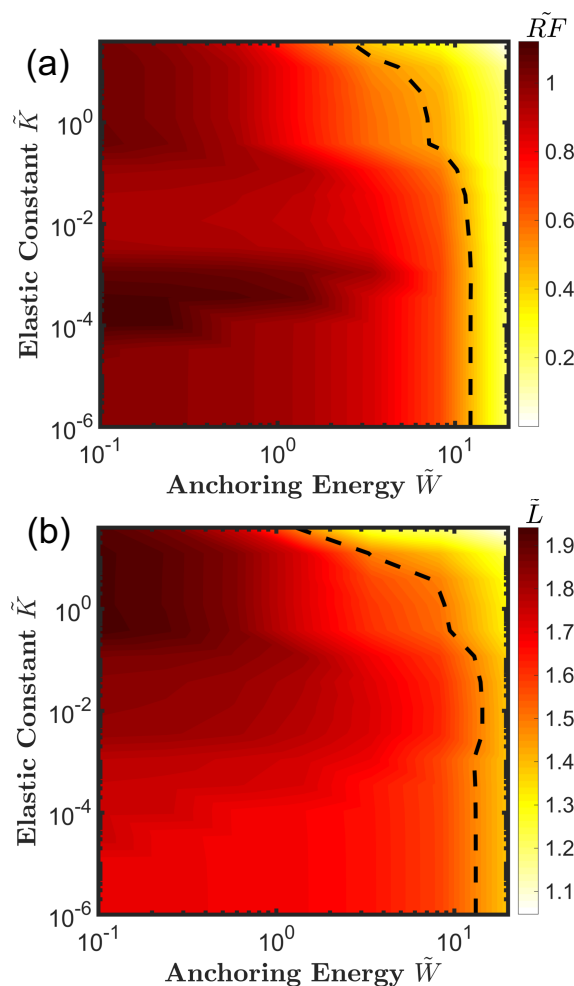


Fig. 4. Effect of elastic constant K and anchoring energy W on the dendrite suppression metrics: (a) roughness factor $\bar{R}_F = R_F/R_{F0}$ measured at $x_{\max} = 90 \mu\text{m}$ where R_{F0} is the roughness using the standard electrolyte (b) arc length ratio \bar{L} measured at $x_{\max} = 120 \mu\text{m}$. The anchoring energy affects the dendrite suppression capability of the LC electrolyte much more than the elastic constant. The contour lines marks $\bar{R}_F = 0.5$ and arc length ratio = 1.5.

19. R Khurana, JL Schaefer, LA Archer, GW Coates, Suppression of lithium dendrite growth using cross-linked polyethylene/poly(ethylene oxide) electrolytes: A new approach for practical lithium-metal polymer batteries. *J. Am. Chem. Soc.* **136**, 7395–7402 (2014).
20. N Li, et al., Suppressing dendritic lithium formation using porous media in lithium metal-based batteries. *Nano Lett.* **18**, 2067–2073 (2018).
21. P Barai, K Higa, V Srinivasan, Lithium dendrite growth mechanisms in polymer electrolytes and prevention strategies. *Phys. Chem. Chem. Phys.* **19**, 20493–20505 (2017).
22. J Li, C Ma, M Chi, C Liang, NJ Dudney, Solid electrolyte: the key for high-voltage lithium batteries. *Adv. Energy Mater.* **5**, 1401408 (2015).
23. A Manthiram, X Yu, S Wang, Lithium battery chemistries enabled by solid-state electrolytes. *Nat. Rev. Mater.* **2**, 16103 (2017).
24. C Monroe, J Newman, The impact of elastic deformation on deposition kinetics at lithium/polymer interfaces. *J. Electrochem. Soc.* **152**, A396–A404 (2005).
25. Z Ahmad, V Viswanathan, Stability of electrodeposition at solid-solid interfaces and implications for metal anodes. *Phys. Rev. Lett.* **119**, 056003 (2017).
26. Z Ahmad, V Viswanathan, Role of anisotropy in determining stability of electrodeposition at solid-solid interfaces. *Phys. Rev. Mater.* **1**, 055403 (2017).
27. Z Ahmad, T Xie, C Maheshwari, JC Grossman, V Viswanathan, Machine learning enabled computational screening of inorganic solid electrolytes for suppression of dendrite formation in lithium metal anodes. *ACS Cent. Sci.* **4**, 996–1006 (2018).
28. PG de Gennes, *The physics of liquid crystals*. (Clarendon Press, Oxford), (1974).
29. G Meier, E Sackmann, JG Grabmaier, *Applications of Liquid Crystals*. (Springer Berlin Heidelberg), (1975).
30. T Kato, From nanostructured liquid crystals to polymer-based electrolytes. *Angewandte Chemie Int. Ed.* **49**, 7847–7848 (2010).
31. H Shimura, et al., Electric-field-responsive lithium-ion conductors of propylenecarbonate-based columnar liquid crystals. *Adv. Mater.* **21**, 1591–1594 (2009).
32. K Kishimoto, et al., Nano-segregated polymeric film exhibiting high ionic conductivities. *J.*

- Am. Chem. Soc.* **127**, 15618–15623 (2005).
33. Z Gadjourova, YG Andreev, DP Tunstall, PG Bruce, Ionic conductivity in crystalline polymer electrolytes. *Nature* **412**, 520–523 (2001).
34. RL Kerr, SA Miller, RK Shoemaker, BJ Elliott, DL Gin, New type of Li ion conductor with 3d interconnected nanopores via polymerization of a liquid organic electrolyte-filled lyotropic liquid-crystal assembly. *J. Am. Chem. Soc.* **131**, 15972–15973 (2009).
35. CT Imrie, MD Ingram, GS McHattie, Ion transport in glassy side-group liquid crystalline polymer electrolytes. *Adv. Mater.* **11**, 832–834 (1999).
36. MA Zimmerman, Solid electrolyte high energy battery (2017) US Patent 9,819,053.
37. MA Zimmerman, AB Gavrilov, Solid, ionically conducting polymer material, and methods and applications for same (2017) US Patent 9,742,008.
38. J Sakuda, et al., Liquid-crystalline electrolytes for lithium-ion batteries: Ordered assemblies of a mesogen-containing carbonate and a lithium salt. *Adv. Funct. Mater.* **25**, 1206–1212 (2015).
39. DW Berreman, Solid surface shape and the alignment of an adjacent nematic liquid crystal. *Phys. Rev. Lett.* **28**, 1683–1686 (1972).
40. DW Berreman, Alignment of liquid crystals by grooved surfaces. *Mol. Cryst. Liq. Cryst.* **23**, 215–231 (1973).
41. B Jerome, Surface effects and anchoring in liquid crystals. *Rep. Prog. Phys.* **54**, 391–451 (1991).
42. M Bouchiat, D Langevin-Cruchon, Molecular order at the free surface of a nematic liquid crystal from light reflectivity measurements. *Phys. Lett. A* **34**, 331–332 (1971).
43. J Stelzer, L Longa, HR Trebin, Rapini-papular constants in a model nematic liquid crystal. *Mol. Cryst. Liq. Cryst. Technol. Sect. A. Mol. Cryst. Liq. Cryst.* **304**, 259–263 (1997).
44. A Rapini, M Papular, Distorsion d'une lamelle nématique sous champ magnétique conditions d'ancrage aux parois. *Le J. de Physique Colloques* **30**, C4–54–C4–56 (1969).
45. A Karma, WJ Rappel, Quantitative phase-field modeling of dendritic growth in two and three dimensions. *Phys. Rev. E* **57**, 4323–4349 (1998).
46. LQ Chen, Phase-field models for microstructure evolution. *Annu. Rev. Mater. Res.* **32**, 113–140 (2002).
47. WJ Boettinger, JA Warren, C Beckermann, A Karma, Phase-field simulation of solidification. *Annu. Rev. Mater. Res.* **32**, 163–194 (2002).
48. JA Warren, R Kobayashi, AE Lobkovsky, WC Carter, Extending phase field models of solidification to polycrystalline materials. *Acta Mater.* **51**, 6035 – 6058 (2003).
49. L Chen, et al., Modulation of dendritic patterns during electrodeposition: A nonlinear phase-field model. *J. Power Sources* **300**, 376 – 385 (2015).
50. DA Cogswell, Quantitative phase-field modeling of dendritic electrodeposition. *Phys. Rev. E* **92**, 011301 (2015).
51. DR Ely, A Jana, RE García, Phase field kinetics of lithium electrodeposits. *J. Power Sources* **272**, 581 – 594 (2014).
52. MZ Bazant, Theory of chemical kinetics and charge transfer based on nonequilibrium thermodynamics. *Acc. Chem. Res.* **46**, 1144–1160 (2013).
53. Z Hong, V Viswanathan, Phase-field simulations of lithium dendrite growth with open-source software. *ACS Energy Lett.* **3**, 1737–1743 (2018).
54. D Gaston, C Newman, G Hansen, D Lebrun-Grandié, Moose: A parallel computational framework for coupled systems of nonlinear equations. *Nucl. Eng. Des.* **239**, 1768 – 1778 (2009).
55. D Schwen, L Aagesen, J Peterson, M Tonks, Rapid multiphase-field model development using a modular free energy based approach with automatic differentiation in moose/marmot. *Comput. Mater. Sci.* **132**, 36 – 45 (2017).
56. M Plapp, Unified derivation of phase-field models for alloy solidification from a grand-potential functional. *Phys. Rev. E* **84**, 031601 (2011).
57. JW Cahn, JE Hilliard, Free energy of a nonuniform system. III. nucleation in a two-component incompressible fluid. *J. Chem. Phys.* **31**, 688–699 (1959).
58. JW Diggle, AR Despic, JO Bockris, The mechanism of the dendritic electrocrystallization of zinc. *J. Electrochem. Soc.* **116**, 1503–1514 (1969).
59. C Monroe, J Newman, The effect of interfacial deformation on electrodeposition kinetics. *J. Electrochem. Soc.* **151**, A880–A886 (2004).
60. RM McMeeking, M Ganser, M Klinsmann, FE Hildebrand, Metal electrode surfaces can roughen despite the constraint of a stiff electrolyte. *J. Electrochem. Soc.* **166**, A984–A995 (2019).
61. A Jana, RE García, Lithium dendrite growth mechanisms in liquid electrolytes. *Nano Energy* **41**, 552–565 (2017).
62. D Demus, J Goodby, GW Gray, HW Spiess, V Vill, *Handbook of Liquid Crystals Set.* (Wiley), (1998).
63. Y Zhu, et al., Design principles for self-forming interfaces enabling stable lithium metal anodes. *arXiv:1903.09593* (22 March 2019).
64. P Albertus, S Babinec, S Litzelman, A Newman, Status and challenges in enabling the lithium metal electrode for high-energy and low-cost rechargeable batteries. *Nat. Energy* **3**, 16–21 (2018).
65. M Rosso, T Gobron, C Brissot, JN Chazalviel, S Lascaud, Onset of dendritic growth in lithium/polymer cells. *J. Power Sources* **97-98**, 804–806 (2001).
66. J Tan, EM Ryan, Structured electrolytes to suppress dendrite growth in high energy density batteries. *Int. J. Energy Res.* **40**, 1800–1810 (2016).
67. A Pizzirusso, R Berardi, L Muccioli, M Ricci, C Zannoni, Predicting surface anchoring: molecular organization across a thin film of 5CB liquid crystal on silicon. *Chem. Sci.* **3**, 573–579 (2012).
68. G van Anders, D Klotsa, NK Ahmed, M Engel, SC Glotzer, Understanding shape entropy through local dense packing. *Proc. Natl. Acad. Sci. U.S.A.* **111**, E4812–E4821 (2014).
69. L Weng, et al., Anchoring energy enhancement and pretilt angle control of liquid crystal alignment on polymerized surfaces. *AIP Adv.* **5**, 09218 (2015).
70. Bw Lee, NA Clark, Alignment of liquid crystals with patterned isotropic surfaces. *Science* **291**, 2576–2580 (2001).
71. C Gear, K Diest, V Liberman, M Rothschild, Engineered liquid crystal anchoring energies with nanopatterned surfaces. *Opt. Express* **23**, 807 (2015).

Supplementary Information for

Dendrite suppression of metal electrodeposition with liquid crystalline electrolytes

Zeeshan Ahmad, Zijian Hong and Venkatasubramanian Viswanathan

Venkatasubramanian Viswanathan.

E-mail: venkvis@cmu.edu

This PDF file includes:

- Supplementary text
- Figs. S1 to S9
- Tables S1 to S3
- Captions for Movies S1 to S4
- References for SI reference citations

Other supplementary materials for this manuscript include the following:

- Movies S1 to S4

Supporting Information Text

MOOSE simulation parameters

All simulations were performed on a two-dimensional mesh $200\ \mu\text{m}$ by $200\ \mu\text{m}$ in size sampled by 200 by 200 grid points using an adaptive time step of maximum 0.01 s. Numerical integration was performed using the **bdf2** scheme while the system of PDEs was solved using Newton method and the single matrix preconditioner as implemented in MOOSE (1). An overpotential of 200 mV was used for all simulations.

Initial Conditions. The metal electrode is located in the region $0 \leq x \leq 20\ \mu\text{m}$ ($\xi = 1$) and the electrolyte in the region $20\ \mu\text{m} \leq x \leq 200\ \mu\text{m}$ ($\xi = 0$) with the gradual variation represented by a tanh function. The Li mole fraction in the electrolyte is set based on 1 M Li concentration in a carbonate based electrolyte. The director field of the liquid crystal \mathbf{n} is set to $(0, 1)^T$ throughout the electrolyte. The potential is set to -0.2 V on the electrode side and 0 V on the electrolyte side.

Boundary Conditions. In general, Dirichlet boundary conditions are employed for the left and boundaries and Neumann boundary conditions for the top and bottom boundaries. The phase-field variable is set to 1 on the left boundary and 0 on the right boundary. The potential is set to -0.2 V in the left boundary and 0 V at the right boundary. The derivatives of phase-field variable and chemical potential are set to zero at the top and bottom boundaries. This can be ensured through, for example, strong anchoring at the interfaces or generation of grooves perpendicular to the plane of the simulation (2). The boundary condition for the director is $\mathbf{n} = (0, 1)^T$ at the right boundary and \mathbf{n} is parallel to the tangent to the surface of the metal electrode at the interface. The latter boundary condition is imposed using the soft constraint method (3) i.e. by adding the energy contribution due to anchoring to the grand free energy in Eq. (5) in the main text.

Anchoring Energy

We use the form of anchoring energy proposed by Rapini and Papoular (4, 5)

$$F_{\text{anch}} = \frac{1}{2}W[1 - (\mathbf{n} \cdot \mathbf{n}_p)^2] \quad [1]$$

where \mathbf{n}_p is the preferred direction for the liquid crystal director in contact with a surface. This form might be further reduced to $F_{\text{anch}} = -W(\mathbf{n} \cdot \mathbf{n}_p)^2/2$ since the first term is a constant offset to the free energy. In two dimensions, if \mathbf{t} is the preferred direction and $\mathbf{v} \perp \mathbf{t}$, the anchoring free energy may be written as $F_{\text{anch}} = -W(\mathbf{n} \cdot \mathbf{t})^2$ or $F_{\text{anch}} = +W(\mathbf{n} \cdot \mathbf{v})^2/2$ since the two differ only by a constant. The latter form is the one we have used in this work.

Overpotential expression

The overpotential due to the LC electrolyte in terms of its properties is given by:

$$\frac{n\mathcal{F}}{V_M}\eta_{\text{LC}} = \frac{\delta\Omega_{\text{LC}}}{\delta\xi} = \frac{\partial\Omega_{\text{LC}}}{\partial\xi} - \frac{\partial\Omega_{\text{LC}}}{\partial\nabla\xi} - h'(\xi) \left[\frac{1}{2}K(\nabla\mathbf{n})^2 + \chi(\mathbf{n} \cdot \nabla\xi)^2 \right] + 2\chi(1 - h(\xi)) [\text{div}(\mathbf{n})(\mathbf{n} \cdot \nabla\xi) + \mathbf{n} \cdot \nabla(\mathbf{n} \cdot \nabla\xi)]$$

Other Phase-field Equations

In the formalism developed by Plapp (6, 7), the local Li-ion mole fraction can be written in terms of the chemical potential of Li, μ as:

$$c_{\text{Li}^+} = \frac{\exp[(\mu - \epsilon^l)/RT]}{1 + \exp[(\mu - \epsilon^l)/RT]}(1 - h(\xi)) \quad [2]$$

where $\epsilon^l = \mu^{0l} - \mu^{0N}$ is the difference in the chemical potential of Li and neutral components in the electrolyte phase at the standard state. We use l as the superscript for the electrolyte and s for the electrode. The equation for evolution of chemical potential is:

$$\frac{\partial\mu}{\partial t} = \frac{1}{\chi_\mu} \left[\nabla \cdot \frac{Dc_{\text{Li}^+}}{RT}(\nabla\mu + n\mathcal{F}\nabla\phi) - \frac{\partial h(\xi)}{\partial t} \left(c^s \frac{C_m^s}{C_m^l} - c^l \right) \right] \quad [3]$$

where C_m^s and C_m^l are the site densities of Li in the electrode and electrolyte phases, ϕ is the electric potential, n is the number of electrons transferred and c is the concentration of Li. The susceptibility χ_μ is given by

$$\chi_\mu = \frac{\partial c^l}{\partial\mu} [1 - h(\xi)] + \frac{\partial c^s}{\partial\mu} h(\xi) \frac{C_m^s}{C_m^l} \quad [4]$$

For obtaining the electric potential, we solve the conduction equation:

$$\nabla \cdot (\sigma \nabla\phi) = n\mathcal{F}C_m^s \frac{\partial\xi}{\partial t} \quad [5]$$

where $\sigma = \sigma^s h(\xi) + \sigma^l (1 - h(\xi))$ is the electronic conductivity.

Properties of the Electrolytes

1 M LiPF₆ in EC/DMC (1:1 volume ratio) is used for obtaining electrolyte properties like diffusivity D , conductivity σ etc. For the LC electrolyte, the molar volume of Li⁺ is assumed to be 5.022E-05 mol/m³ (8). All properties are tabulated in Table S1.

Table S1. Parameters used in the phase-field model. The code is available from <https://github.com/ahzeeshan/electrodep>

Properties	Value in S.I. units	S.I. Units	Normalized Value
RT	2494.2	J/mol	9.870E-01
γ (9)	0.556	J/m ²	2.200E-01
δ	1.00E-06	m	1.000E+00
κ	8.34E-07	J/m	3.300E-01
b	6.67E+06	J/m ³	2.640E+00
D (10)	3.20E-10	m ² /s	3.197E+02
σ^s	1.0E+07	S/m=A/(Vm)	3.953E+12
σ^l (10)	1.19	S/m=A/(Vm)	4.704E+05
α (11)	0.5	-	0.5
i_0 (12)	15	A/m ²	5.929E+00
L_σ (11)	2.50E-06	m ³ /(Js)	6.318E+00
$L_\eta = \gamma V_{Li} i_0 / \mathcal{F} \kappa$ (7)	1.35E-03	1/s	1.347E-03
\mathcal{F}	9.6485E+04	C/mol	3.814E+01
V_{Li^+} (8)	5.022E-05	m ³ /mol	5.022E-02
V_{Li} (8)	1.30E-05	m ³ /mol	1.300E-02
μ^l	173.1960308	J/mol	6.854E-02
ϵ^l	6565.678657	J/mol	2.598E+00
μ^s	34458.64644	J/mol	1.364E+01
ϵ^s	-34458.64394	J/mol	-1.364E+01
c_0	1.00E+03	mol/m ³	1.000E+00

Property Normalization/Scaling

The normalization constants for the different quantities are presented in Table S2.

Table S2. All variables are normalized using the following values in SI units, e.g. lengths are normalized by 10⁻⁶ m.

Variable	Value
Length	1.00E-06 m
Mass	2.527 kg
Time	1 s
Moles	1.00E-15 mol
Charge	2.53E-12 C
Voltage	1.00E+00 V

Metrics for dendrite suppression

For Fig. 1 (in the main text), if the interface is given by the curve $x = f(y)$, the arc length of the interface can be calculated using $\int dy \sqrt{1 + f'(y)^2}$ which can be converted to a discrete summation.

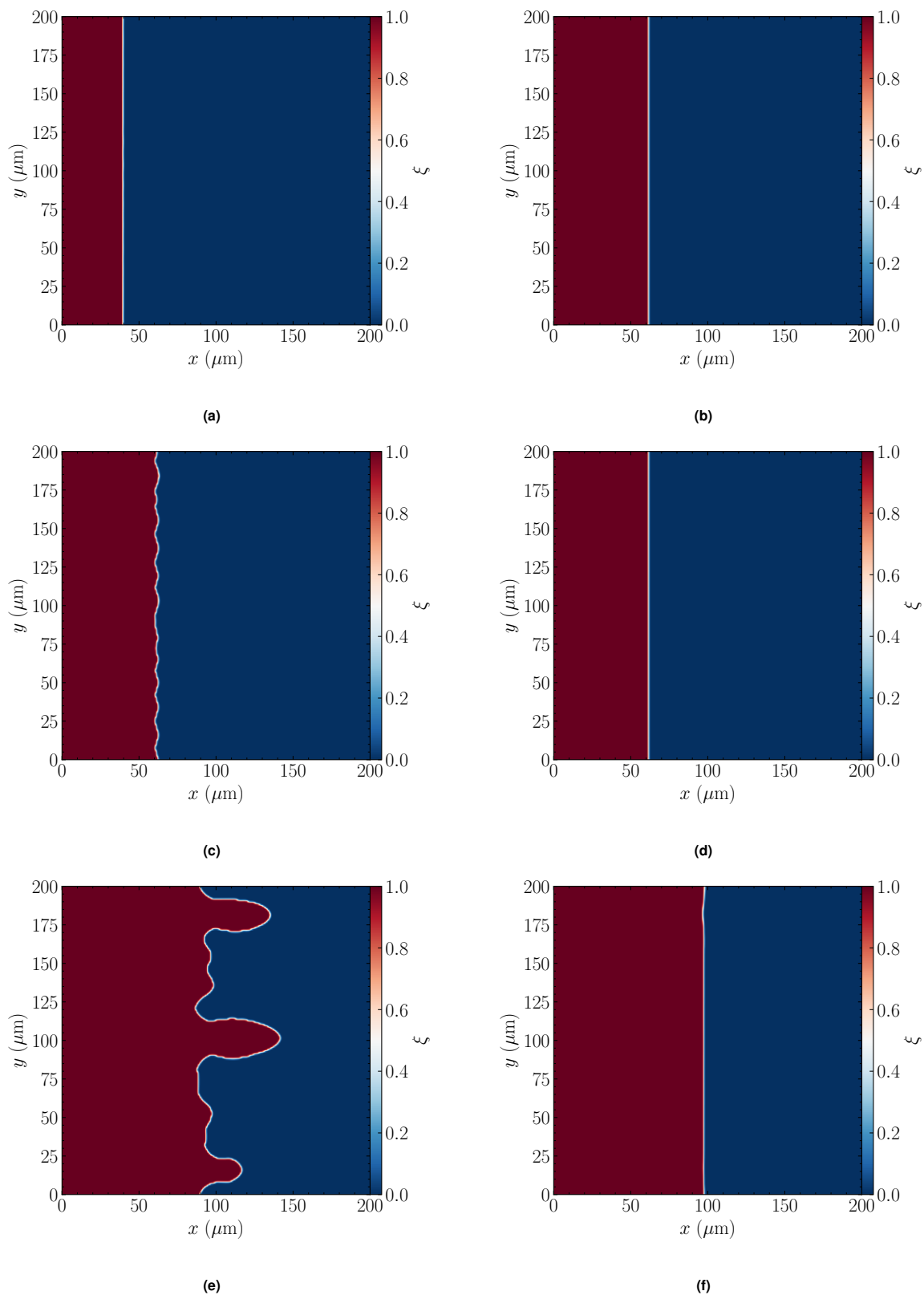


Fig. S1. Growth of metal surface with a standard [(a), (c) and (e)] and LC electrolyte [(b), (d) and (f)] at different times: 100 s [(a), (b)], 200 s [(c), (d)], 330 s [(e), (f)]. It can be seen that the dendrites start to nucleate after 200 s and eventually develop into large dendrites after 330 s with the standard electrolyte. In contrast, the interface is quite stable with the LC electrolyte up to 330 s. This clearly indicates that the LC electrolyte can help suppress dendrite formation.

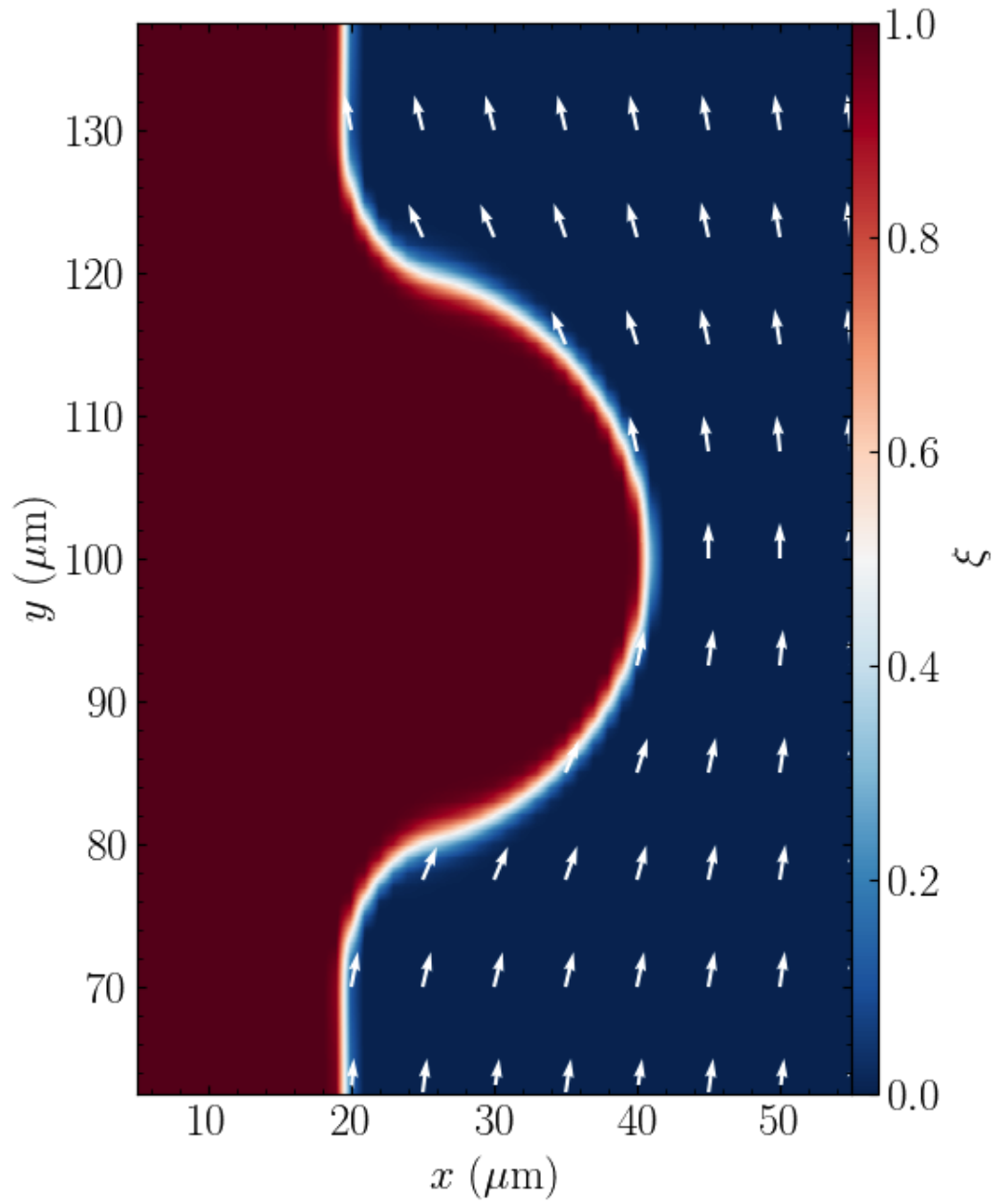
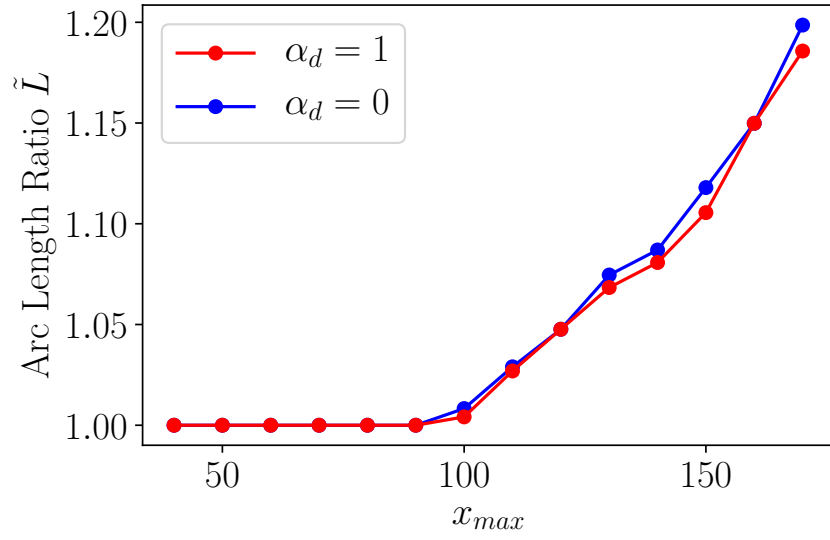
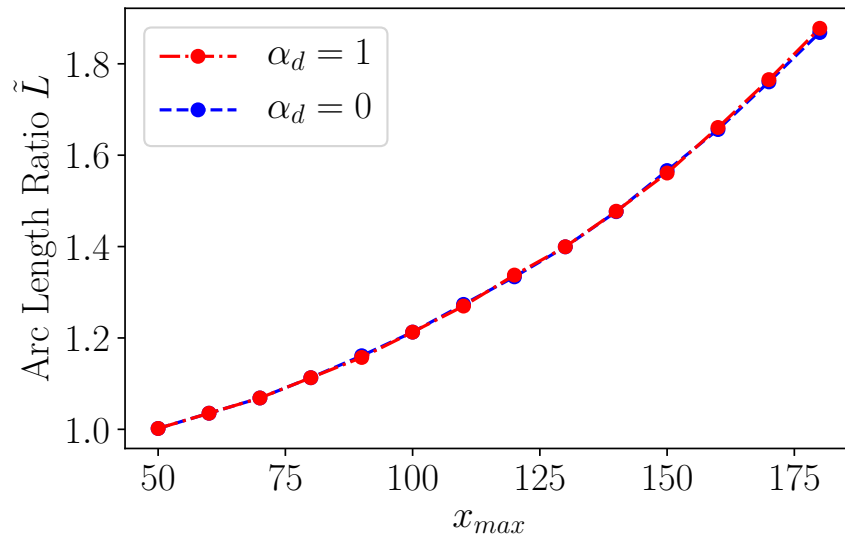


Fig. S2. Distortion of the liquid crystal director field \mathbf{n} due to an initial hemispherical nucleus. The arrows show the spatial distribution of the director field of the liquid crystal in the vicinity of the surface perturbation. It is clearly shown that the director field reorients along the hemispherical nucleus which is caused by the anchoring energy.

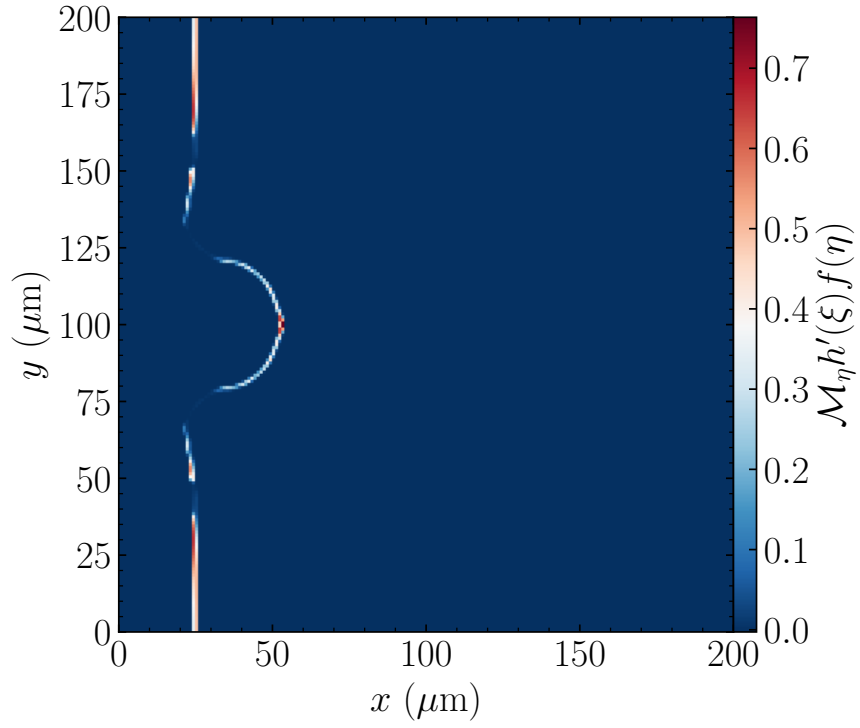


(a)

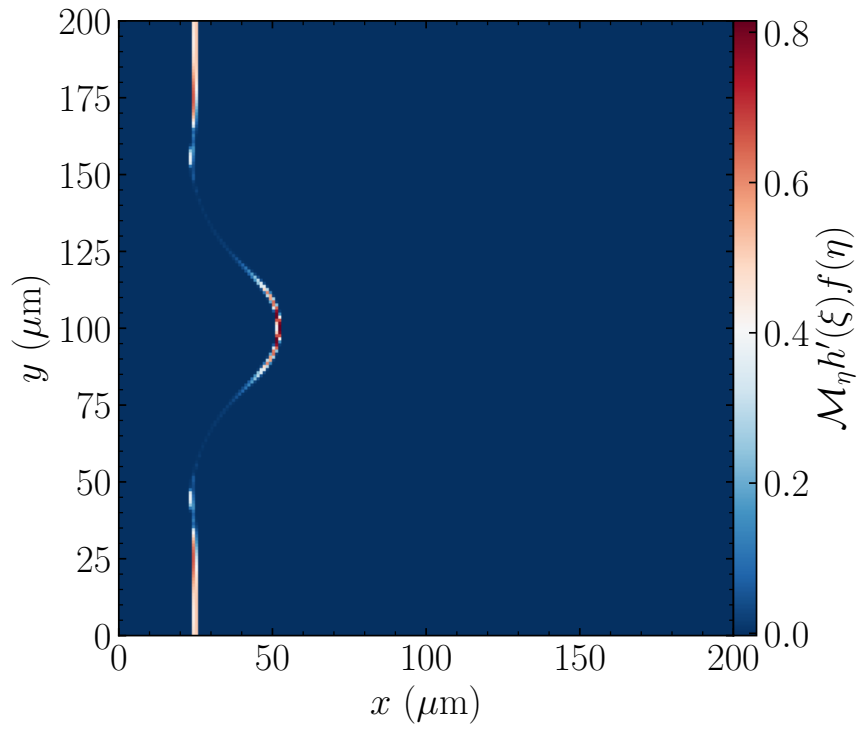


(b)

Fig. S3. Comparison of the arc length ratio \tilde{L} for $\alpha_d = 0$ and 1 for the case of an initial condition of (a) smooth metal surface and (b) $40 \mu\text{m}$ nucleus at the metal surface (same as presented in the main text).



(a)



(b)

Fig. S4. Comparison of the electrodeposition kinetics for the case of (a) standard electrolyte and (b) LC electrolyte at time=31 s. Higher the value of $\mathcal{M}_\eta h'(xi)f(\eta)$, higher is the electrodeposition. The current density is much more localized at the tip of the nucleus in the case of a standard electrolyte compared to the LC electrolyte.

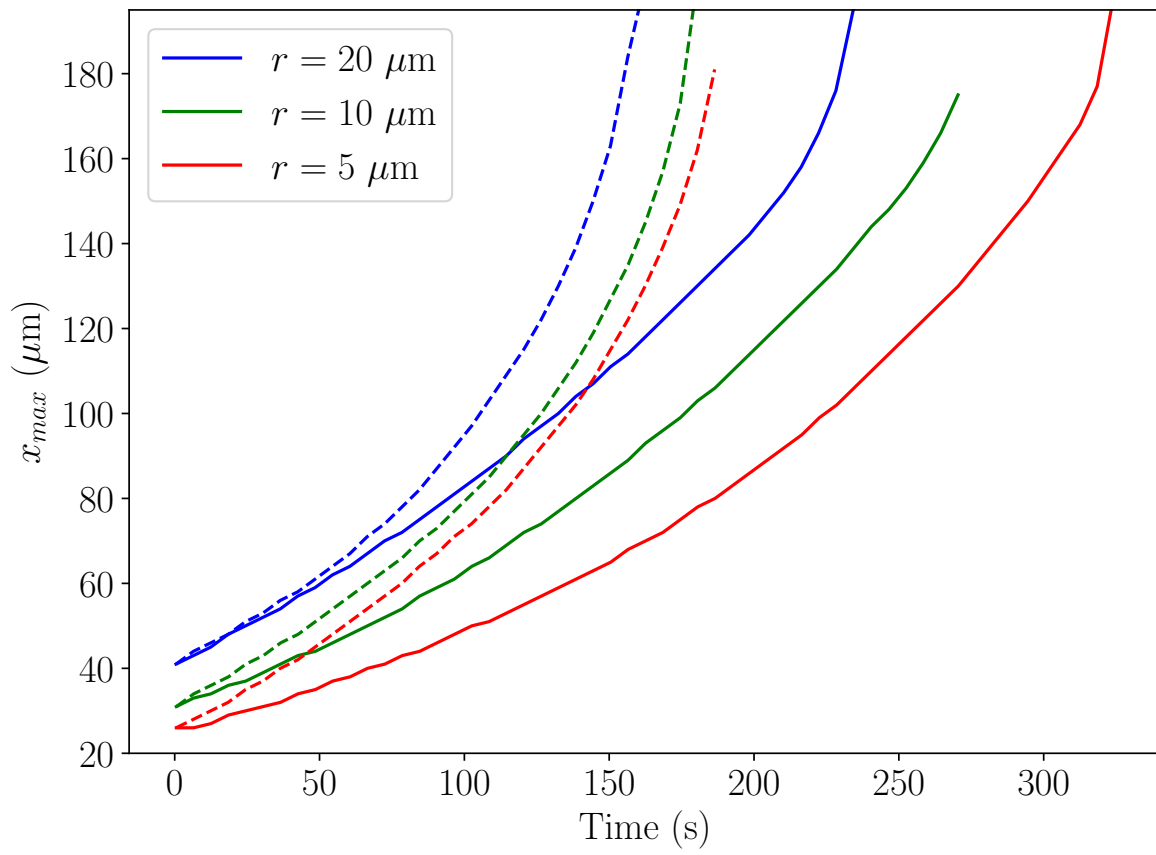


Fig. S5. Evolution of the maximum x-coordinate for a standard electrolyte (dashed line) and LC electrolyte (solid line) with time. The LC electrolyte has a slower growth due to suppression of dendrites.

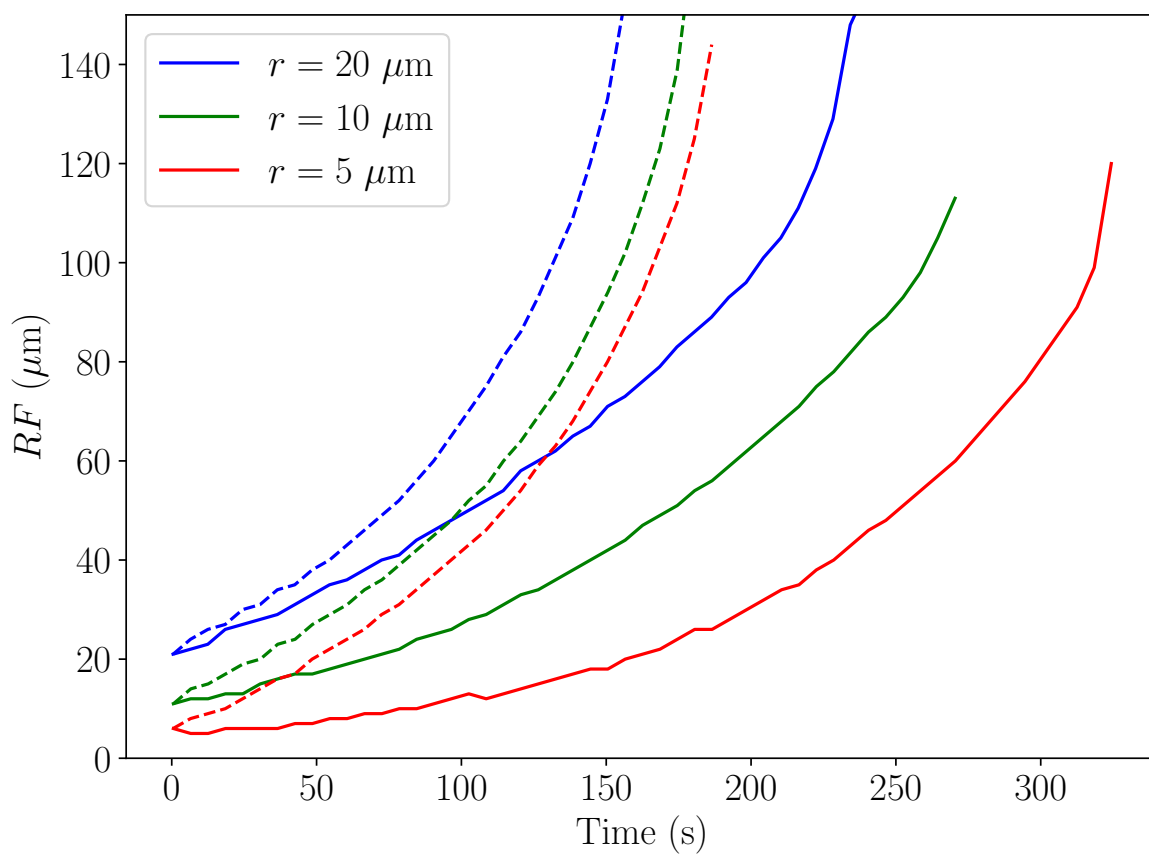


Fig. S6. Evolution of the roughness factor RF for a standard electrolyte (dashed line) and LC electrolyte (solid line) with time.

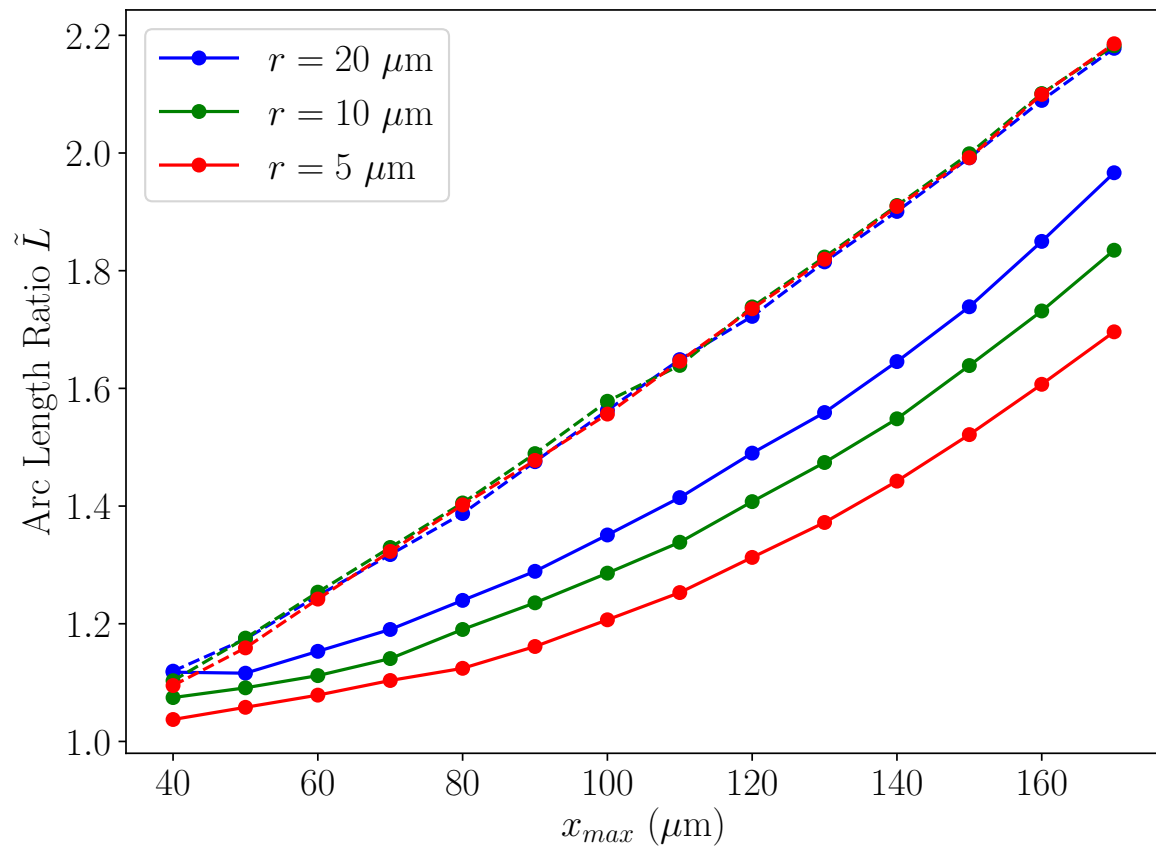


Fig. S7. Evolution of the interface arc length ratio with maximum x-coordinate for a standard electrolyte (dashed line) and LC electrolyte (solid line). The LC electrolyte has a slower growth of the arc length ratio due to suppression of sharp dendritic peaks.

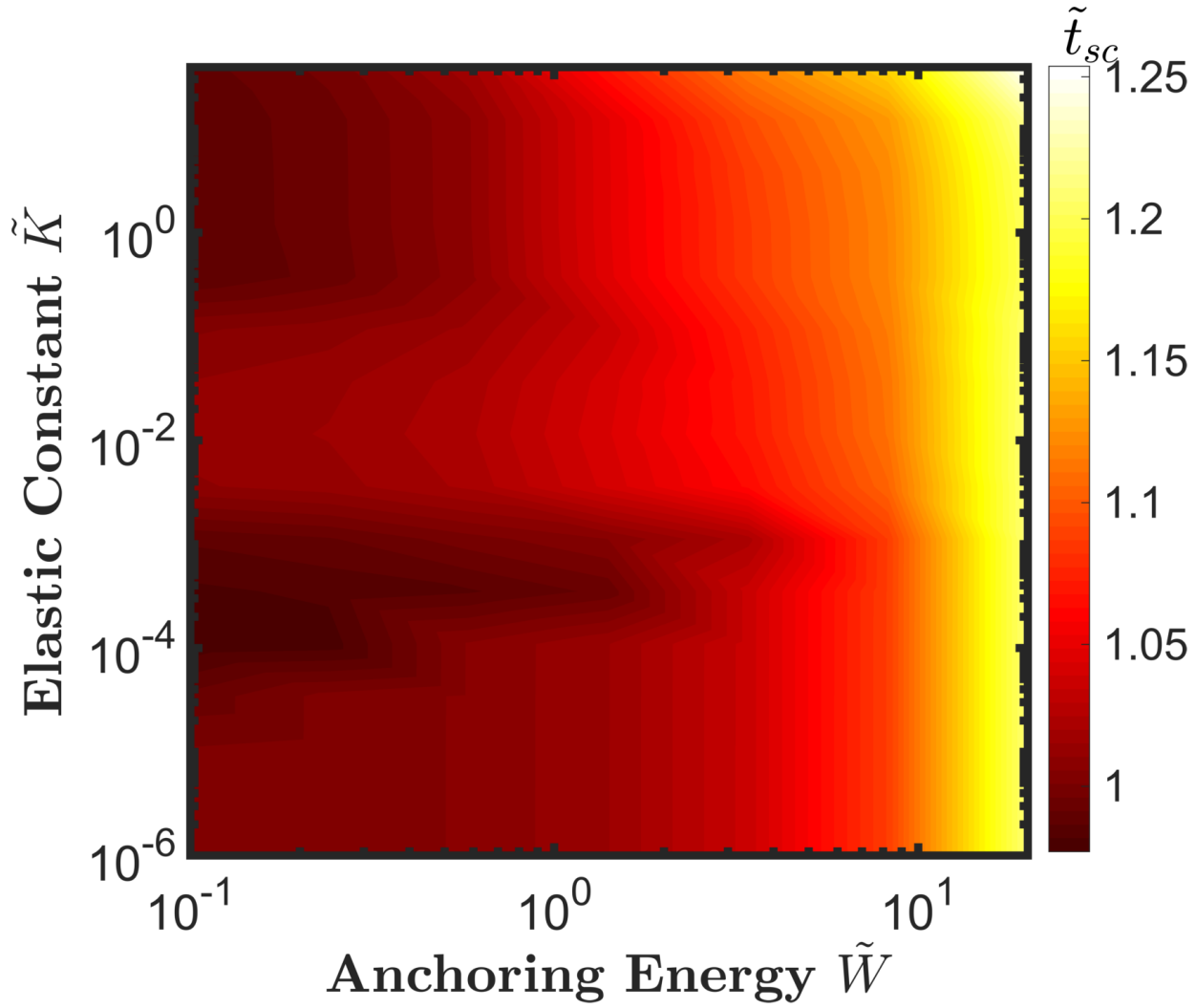
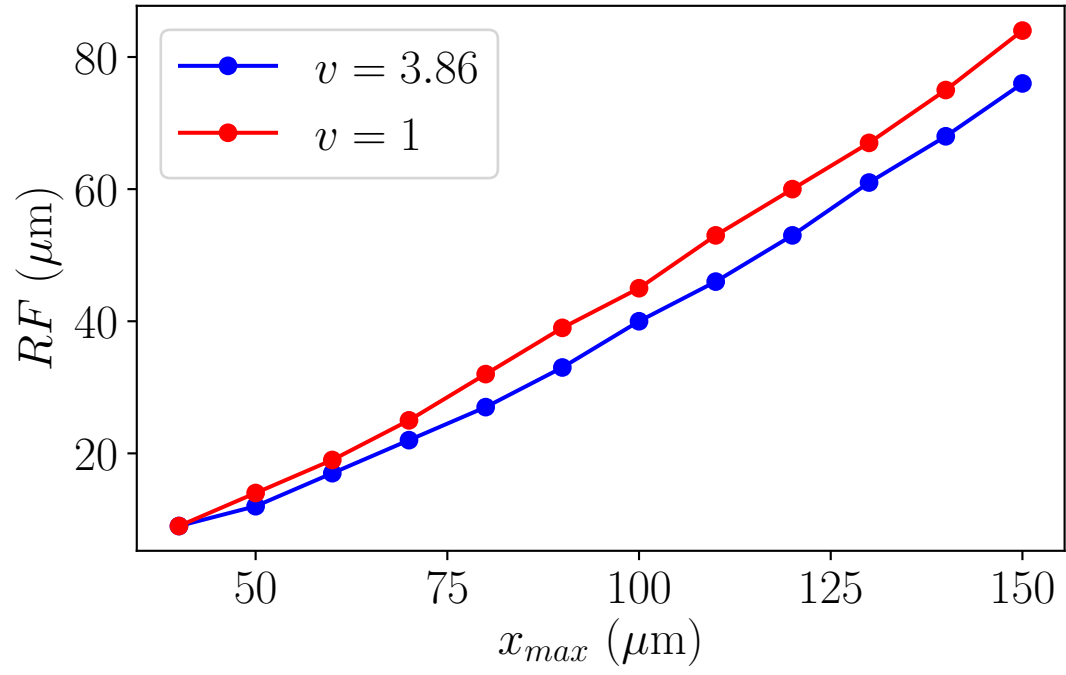
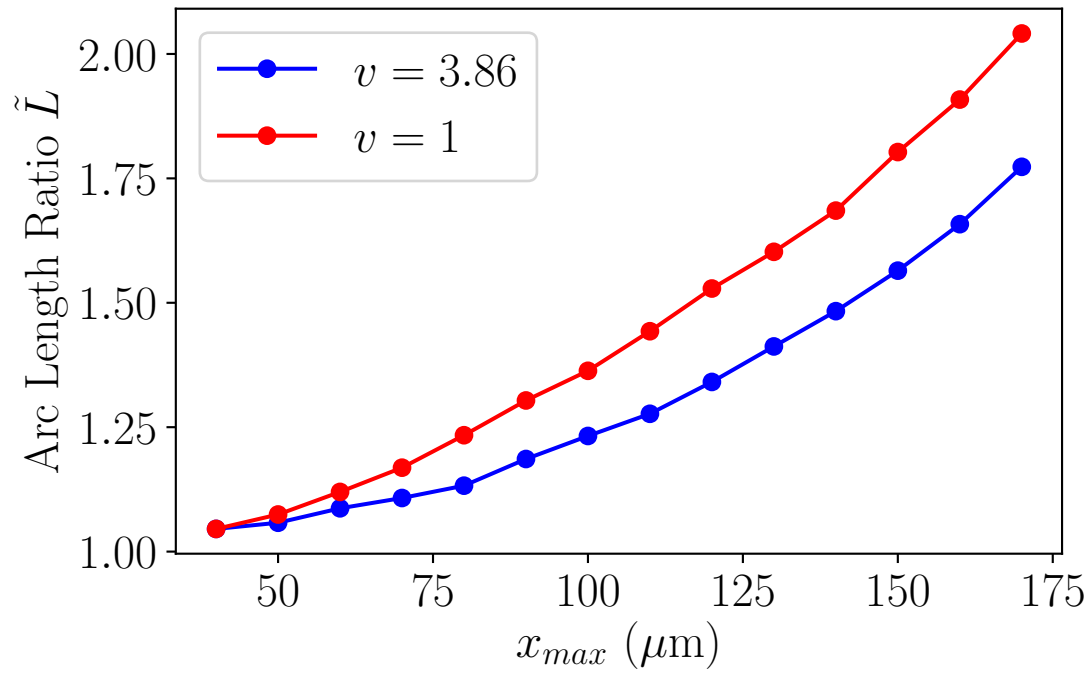


Fig. S8. Effect of elastic constant K and anchoring energy W on the dendrite suppression metrics: short circuit time \tilde{t}_{sc} . The anchoring energy affects the dendrite suppression capability of the liquid crystalline electrolyte much more than the elastic constant. The short circuit time is normalized using the corresponding time obtained for the standard electrolyte. Note that the ideal short circuit time is not infinite and can only be increased to its maximum value obtained when the electrodeposition is perfectly smooth with $RF=0 \mu m$.



(a)



(b)

Fig. S9. Variation of (a) roughness factor and (b) arc length ratio \tilde{L} with the maximum x-coordinate of the metal surface plotted for two different values of molar volume of lithium in the electrolyte. $v = V_{Li^+}/V_{Li}$ is the molar volume ratio. Higher molar volume in the electrolyte results in lower roughness and lower arc length ratio. The initial state has a $5 \mu\text{m}$ radius hemispherical nucleus.

Table S3. Elastic constants of common liquid crystalline materials. Data obtained from Refs. (13–19)

Molecule Name	K_{11} (N)	\tilde{K}_{11} (Normalized)
PAA: p-azoxyanisole	9.00E-12	3.56E-06
MBBA	7.48E-12	2.96E-06
Nematic 5CB: 4-n-pentyl-4-cyano biphenyl	8.00E-12	3.17E-06
Py-7: 5-n-heptyl-2-(4'-cyanophenyl)-pyrimidine.	5.04E-12	1.99E-06
CB-7: 4-n-heptyl-4'-cyanobiphenyl.	8.55E-12	3.38E-06
PCH-7: trans-4-n-heptyl-(4'-cyanophenyl)-cyclohexane.	1.01E-11	4.00E-06
CCH -7: trans, trans -4-n-heptyl:4'-cyanobicyclohexane.	7.24E-12	2.86E-06
C -7: trans-4'-cyanophenyl-4-n-heptylcyclohexanoate.	7.75E-12	3.06E-06
C-5: trans4'-cyanophenyl-4-n-pentylcyclohexanoate.	7.75E-12	3.07E-06
7CB	7.3E-12	2.89E-06
6CB	3.80E-12	1.50E-06

Movie S1. Metal electrodeposition with a standard electrolyte with a smooth initial surface of the metal. The perturbations lead to the growth of three dendrites.

Movie S2. Metal electrodeposition with LC electrolyte with a smooth initial surface of the metal. The LC electrolyte has non-dimensional values of elastic constant $\tilde{K} = 2\tilde{\delta}^2 \tilde{R}\tilde{T}/\tilde{V}_{Li} = 39.3$ and anchoring energy $\tilde{W} = 20$. Dendrites are suppressed in this case.

Movie S3. Metal electrodeposition with a standard electrolyte with a 20 μm radius nucleus at the metal surface.

Movie S4. Metal electrodeposition with an LC electrolyte with 20 μm radius nucleus at the metal surface. The LC electrolyte has non-dimensional values of elastic constant $\tilde{K} = 2\tilde{\delta}^2 \tilde{R}\tilde{T}/\tilde{V}_{Li} = 39.3$ and anchoring energy $\tilde{W} = 20$.

References

1. D Gaston, C Newman, G Hansen, D Lebrun-Grandié, Moose: A parallel computational framework for coupled systems of nonlinear equations. *Nucl. Eng. Des.* **239**, 1768 – 1778 (2009).
2. DW Berreman, Solid surface shape and the alignment of an adjacent nematic liquid crystal. *Phys. Rev. Lett.* **28**, 1683–1686 (1972).
3. D Schwen, L Aagesen, J Peterson, M Tonks, Rapid multiphase-field model development using a modular free energy based approach with automatic differentiation in moose/marmot. *Comput. Mater. Sci.* **132**, 36 – 45 (2017).
4. J Stelzer, L Longa, HR Trebin, Rapini-papoular constants in a model nematic liquid crystal. *Mol. Cryst. Liq. Cryst. Sci. Technol. Sect. A. Mol. Cryst. Liq. Cryst.* **304**, 259–263 (1997).
5. A Rapini, M Papoular, Distorsion d'une lamelle nématique sous champ magnétique conditions d'ancrage aux parois. *Le J. de Physique Colloques* **30**, C4-54–C4-56 (1969).
6. M Plapp, Unified derivation of phase-field models for alloy solidification from a grand-potential functional. *Phys. Rev. E* **84**, 031601 (2011).
7. Z Hong, V Viswanathan, Phase-field simulations of lithium dendrite growth with open-source software. *ACS Energy Lett.* **3**, 1737–1743 (2018).
8. C Monroe, J Newman, The impact of elastic deformation on deposition kinetics at lithium/polymer interfaces. *J. Electrochem. Soc.* **152**, A396–A404 (2005).
9. L Vitos, A Ruban, H Skriver, J Kollár, The surface energy of metals. *Surf. Sci.* **411**, 186 – 202 (1998).
10. LO Valøen, JN Reimers, Transport properties of LiPF6-based Li-ion battery electrolytes. *J. The Electrochem. Soc.* **152**, A882–A891 (2005).
11. L Chen, et al., Modulation of dendritic patterns during electrodeposition: A nonlinear phase-field model. *J. Power Sources* **300**, 376 – 385 (2015).
12. F Shi, et al., Strong texturing of lithium metal in batteries. *Proc. Natl. Acad. Sci. U.S.A.* **114**, 12138–12143 (2017).
13. D Demus, J Goodby, GW Gray, HW Spiess, V Vill, *Handbook of Liquid Crystals Set.* (Wiley), (1998).
14. B Tjpto-Margo, GT Evans, MP Allen, D Frenkel, Elastic constants of hard and soft nematic liquid crystals. *J. Phys. Chem.* **96**, 3942–3948 (1992).
15. K Skarp, ST Lagerwall, B Stebler, Measurements of hydrodynamic parameters for nematic 5CB. *Mol. Cryst. Liq. Cryst.* **60**, 215–236 (1980).
16. WHD Jeu, WAP Claassen, AMJ Spruijt, The determination of the elastic constants of nematic liquid crystals. *Mol. Cryst. Liq. Cryst.* **37**, 269–280 (1976).
17. H Schad, MA Osman, Elastic constants and molecular association of cyano-substituted nematic liquid crystals. *The J. Chem. Phys.* **75**, 880–885 (1981).
18. NV Madhusudana, R Pratibha, Elasticity and orientational order in some cyanobiphenyls: Part IV. reanalysis of the data. *Mol. Cryst. Liq. Cryst.* **89**, 249–257 (1982).
19. A Pizzirusso, R Berardi, L Muccioli, M Ricci, C Zannoni, Predicting surface anchoring: molecular organization across a thin film of 5CB liquid crystal on silicon. *Chem. Sci.* **3**, 573–579 (2012).